

PCCP

Accepted Manuscript



This is an *Accepted Manuscript*, which has been through the Royal Society of Chemistry peer review process and has been accepted for publication.

Accepted Manuscripts are published online shortly after acceptance, before technical editing, formatting and proof reading. Using this free service, authors can make their results available to the community, in citable form, before we publish the edited article. We will replace this *Accepted Manuscript* with the edited and formatted *Advance Article* as soon as it is available.

You can find more information about *Accepted Manuscripts* in the [Information for Authors](#).

Please note that technical editing may introduce minor changes to the text and/or graphics, which may alter content. The journal's standard [Terms & Conditions](#) and the [Ethical guidelines](#) still apply. In no event shall the Royal Society of Chemistry be held responsible for any errors or omissions in this *Accepted Manuscript* or any consequences arising from the use of any information it contains.

Fabrication of nanoscale heterostructures comprised of graphene-encapsulated gold nanoparticles and semiconducting quantum dots for photocatalysis

Cite this: DOI: 10.1039/x0xx00000x

Yuan Li,^a and Nitin Chopra^{a,b,c*}

Received 00th January 2012,
Accepted 00th January 2012

DOI: 10.1039/x0xx00000x

www.rsc.org/

Patterned growth of multilayer graphene shell encapsulated gold nanoparticles (GNPs) and their covalent linking with inorganic quantum dots is demonstrated. GNPs were grown using a xylene chemical vapor deposition process, where surface oxidized gold nanoparticles catalyze the multilayer graphene shell growth in a single step process. The graphene shell encapsulating gold nanoparticles could be further functionalized with carboxylic groups, which were covalently linked to amine-terminated quantum dots resulting in GNP-quantum dot heterostructures. The compositions, morphologies, crystallinity, and surface functionalization of GNPs and their heterostructures with quantum dots were evaluated using microscopic, spectroscopic, and analytical methods. Furthermore, optical properties of the derived architectures were studied using both, experimental methods and simulations. Finally, GNP-quantum dot heterostructures were studied for photocatalytic degradation of phenol.

1. Introduction

Efficient photocatalytic degradation of organic pollutants using nanostructured photocatalysts has been considered as one of the most promising and sustainable strategies for water cleaning and environment remediation.¹⁻³ However, the long-term industrial scale photodegradation is still limited due to various shortcuts of the currently-used photocatalysts (e.g., metal oxides and sulfides) including wide band gap energies, rapid recombination of excited charge carriers, and/or poor (electro)chemical stability.^{4,5} With this regard, the combination of these semiconductor photocatalysts with noble metal nanostructures such as gold (Au) and silver (Ag) was found to be capable to result in band gap modulation and catalytic efficiency improvement.^{6,7} This could be attributed to the strong light-matter interactions and efficient energy or charge transfer between Au or Ag nanostructures and semiconductors.^{8,9} These interaction and charge transfer process have significant distance dependence, and thus the effective combination or contacting between noble metals and semiconductors becomes of great importance and is still the main challenge due to the lack of binding chemistry on noble metals.^{10,11}

Carbon nanostructures such as carbon nanotubes (CNTs), graphene, etc. exhibit a diverse range of surface chemistry necessary for developing hierarchical heterostructures.^{12,13} The combination of these carbon nanostructures with nanoparticles/quantum dots has been performed for defect labeling, sensors, and surface chemical analysis.^{14,15} For instance, chemically-exfoliated graphene wrapped around Au nanoparticles has been reported for biosensors and bioelectronics.¹⁶ However, the corrosive nature of the exfoliation process and the inability of

wrapped graphene to form an impervious shell around Au nanoparticles limited their electrical transport and did not completely prevent exposure of the encapsulated Au nanoparticle. Thus, spherical carbon nanostructures such as fullerene, onion-like carbon (OLC), and carbon nanocapsules hold great potential.^{17,18} The morphology, dimension, and surface functionality of spherical carbon nanostructures can result in tunable properties, which can be further modulated by the loaded nanostructures. For instance, heterostructures comprised of spherical carbon nanostructures loaded with quantum dots have been reported to be a promising electron donor-acceptor system for energy harvesting.^{19,20}

With this regard, a novel configuration can be developed as multilayer graphene shell encapsulated Au nanoparticles coordinated with quantum dots. Here, the shell provides a robust surface passivation to the encapsulated Au nanoparticle and also serves as a multifunctional interface between the Au nanoparticle and the extraneous quantum dots. Past research in the growth of carbon shells on Au nanoparticles has been mainly focused on in-situ TEM based synthesis by converting lacey carbon on TEM grids to a graphitic shell around the Au nanoparticles or pyrolysis of polymer coatings around the Au nanoparticles.^{21,22} However, the former method resulted in difficulty in the extraction of hybrid nanoparticles from the TEM grid while the latter approach involved tedious cleaning steps to remove amorphous carbon from the encapsulated Au nanoparticles. Recently, the authors demonstrated a facile and scalable xylene-based Chemical Vapor Deposition (CVD) approach for the growth of multilayer graphene shell on Au nanoparticles (referred as graphene nanoparticles or GNPs).²³⁻²⁵ The presence of multilayer graphene shell modulated or improved the optical

properties and chemical stability of the Au nanoparticles.²⁶ Most importantly, this process gives Au nanoparticles enriched carbon-based surface chemistry, allowing their further surface functionalization and heterostructuring.²⁵

The functionalization of carbon materials with extraneous nanocrystals can be simply achieved *via* an in-situ approach,^{12,20} where these foreign nanostructures were attached to the surface of carbon by heterogeneous nucleation during their synthesis process. The main disadvantage of this process is the lack of control on the size, shape and positioning of the nanocrystals. This leads to the development of strategies which first synthesized the nanocrystal in a separate process and then attached them to carbon materials *via* a non-covalent^{27,28} or covalent approach.^{29,30} The non-covalent approach was limited also due to the weak binding force and inability of selective positioning. Thus, the covalent approach is widely-preferred for the functionalization of carbon materials. The main advantages of such covalent approaches including (1) the shape and size of hybridizing nanocrystals can be tailored by the sophisticated synthesis before connecting to carbon surface,¹² (2) reliable and robust chemical bonds formed between carbon and hybridizing nanostructures, which can even stand for strong sonication or extensive washing; (3) the spatial coverage and exact positioning of extraneous nanostructures can be precisely controlled by the specific functionalities on carbon surface.¹⁴

Accordingly, in this paper we report a facile and controlled approach for the assembly of fluorescent CdS_xSe_{1-x}/ZnS quantum dots onto the multilayer graphene shell-encapsulated Au nanoparticles, resulting a complex GNP-QD heterostructures with novel plasmonic properties and enhanced charge transfer efficiency. Briefly, uniformly-dispersed Au nanoparticles were formed on a silicon (Si) substrate, followed by the CVD growth multilayer graphene shell as we reported before.^{23,24} Further plasma or acid treatment of the patterned GNPs resulted in carboxylic (-COOH) group derivatization on the multilayer graphene shell. The (-COOH)-derivatized GNPs were covalently and selectively linked with amine (-NH₂)-terminated quantum dots using the well-defined carbodiimide chemistry.²⁵ The GNP-QD heterostructures were evaluated for their binding chemistry, phases, structure, and morphology using spectroscopic, diffraction, and microscopic methods. Their band gap energies, and their optical, electrical, and photocatalytic properties were also demonstrated.

2. Experimental

2.1 Materials and Methods

Si substrate (111) was purchased from IWS (Colfax, CA). Potassium gold (III) chloride was purchased from Sigma-Aldrich (St. Louis, MO). Hydrogen fluoride (~50 wt.%) was purchased from VWR (Atlanta, GA). Ammonium fluoride was purchased from Alfa Aesar (Ward Hill, MA). 1-ethyl-3-(3-dimethylaminopropyl) carbodiimide (EDC), N-hydroxysuccinimide (NHS), and 2-(N-morpholino) ethanesulfonic acid (MES) were purchased from Thermo scientific (Rockford, IL). (-NH₂)-terminated CdSe_xS_{1-x}/ZnS fluorescent quantum dots were purchased from Cytodiagnosics Inc. (Burlington, Canada). All chemicals were used as such. Buffered oxide etch (BOE) solution was prepared by mixing NH₄F and HF in DI-water. DI-water (18.1 MΩ-cm) was obtained from a Barnstead International DI-water system (E-pure D4641). The GNP growth was carried out in a Lindberg blue three-zone tube furnace (Water-town, WI) with the quartz tube purchased from ChemGlass

(Vineland, NJ). Oxygen plasma was performed in Nordson March Jupiter III Reactive Ion Etcher (Concord, CA).

2.2 Patterning of GNPs and their carboxylic derivatization

Au film was deposited on the Si substrate using an acid-based wet-chemical method.³⁷ In this method, cleaned Si substrate was treated with BOE solution to remove the surface oxide layer. This was followed by immersing the substrate in an acidic solution comprised of ~1 mM KAuCl₄ and 1% HF. This reaction resulted in Au film (~20 nm thick) on the Si substrate. The substrate was washed with DI-water, dried, and annealed in air for 15 min at 850 °C to dewet Au film that resulted in Au nanoparticles patterned on the Si substrate.

CVD process was employed for the growth of multilayer graphene shell.²³ First, Au nanoparticles patterned on Si substrate were treated with oxygen plasma for 15 min to result in surface gold oxide.²³ This was followed by CVD growth of multilayer graphene shell between 600 and 700 °C for 1 h. Xylene was utilized as the carbon source. The carrier gas was H₂/Ar with a flow rate of 1.15 SLM. This process resulted in patterned growth of GNPs on the Si substrate. The -COOH derivatization on the GNPs was carried out by treating the as-grown GNPs with oxygen plasma for 15 s. In order to compare the plasma oxidation-based derivatization process, nitric acid treatment was also carried out for the as-produced GNPs. This involved treatment of the Si substrate with patterned GNPs in a 3 M HNO₃ solution at 60 °C for 5 h.

2.3 Covalent binding of quantum dots on GNPs

The binding approach employed the well-established carbodiimide chemistry.^{25,31} The Si substrate patterned with (-COOH)-terminated GNPs was immersed in a ~50 mM MES buffer solution with ~2 mM EDC and incubated for 10 min. This was followed by the addition of ~4 mM NHS. This process allowed the formation of a stable amine-reactive NHS ester. The substrate was washed with PBS buffer (pH = 7.4) and then immersed in the same solution containing 2 mM quantum dots. This reaction continued for 12 h to form amide bonds (-CONH-) between the GNPs and quantum dots, resulting in covalently linked GNP-QD heterostructures. Finally, the substrate with patterned assembly of GNP-QD heterostructures was washed with DI-water and dried in N₂. This washing step removed physically adsorbed quantum dots from the surface of Si substrate and patterned GNPs.

2.4. Optical properties, plasmonic modeling and photocatalytic degradation of phenol

The optical transition energy for the pristine quantum dots and the GNP-QD heterostructures was further determined using equation (1),^{32,33}

$$ahv = A(hv - E_g)^n, \quad (1)$$

where a is absorbance coefficient, A is a constant, $h\nu$ is the energy of light and n is a constant depending on the nature of the electron transition (n is 1/2, 2, 3/2 and 3 for allowed direct, allowed indirect, forbidden direct and forbidden indirect transitions, respectively). CdS_xSe_{1-x}/ZnS quantum dots have been reported as an allowed direct band gap semiconductor.³⁴ Thus, the optical band gap energies were calculated by extrapolating the linear portion of the Tauc plots [$(ahv)^2$ vs. $h\nu$] to the $h\nu$ -axis where $(ahv)^2 = 0$.

Discrete dipole approximation (DDA) method²⁶ was used to simulate the plasmonic properties (scattering and absorbance)

of the as-produced Au nanoparticles, GNPs (before and after plasma treatment), and GNP-QD heterostructures. This method is based on the solution of the 3D Maxwell equation *via* the DDSCAT code developed by Draine and Flatau.³⁵ Detailed simulation procedures have been demonstrated earlier by the authors.²⁶ Briefly, DDSCAT 7.2 was utilized to estimate the normalized electric field or surface plasmon generation for all these mentioned samples or targets. The normalized electric field intensity is defined as the ratio between the electric field generated near the target surface and the incident electric field ($|E|/|E_0|$). The geometrical targets were generated using 3D max software for various simulated nanostructures. The effective radius of the dipoles was calculated using: $r_{\text{eff}} = (3V/4\pi)^{1/3}$, where V is the total volume of the target and is calculated with $V = Nd^3$ (N is the number of dipoles and d is the lattice spacing in cubic array).

To demonstrate the photocatalytic activity, Si substrates (2 cm × 2 cm) patterned with the as-produced GNPs or GNP-QD heterostructures were sonicated to disperse the nanostructures in DI-water. In the following, ~0.2 mL of phenol (3 mM) was added into these nanostructure suspensions and sonicated for another 1 min. This was followed by further addition of ~0.1 mL H₂O₂ (37%) as the sacrificial agent.³⁶ A UV illumination lamp (~254 nm, 8W) was utilized as the light source and the solution was gently stirred during the photodegradation experiment. At 30 min intervals, the solution was centrifuged and UV-vis spectra for the supernatant were recorded to estimate the concentration of phenol. The samples were re-dispersed in the supernatant and the degradation experiment and analysis was conducted for 6 h. The same photodegradation process was also conducted using the pristine quantum dots as comparison.

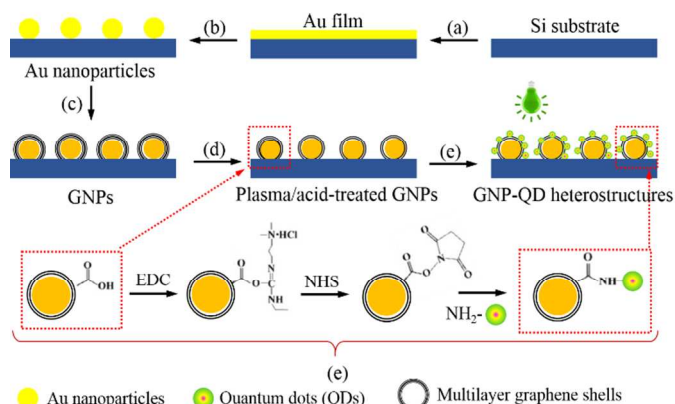
2.5 Characterizations

FE-SEM (JEOL-7000) and Tecnai F-20 TEM were used to characterize the morphology, crystal structure, and/or interfaces present in Au nanoparticles, as-produced GNPs, and GNP-QD heterostructures. X-ray photoelectron spectra (XPS) were gathered by a Kratos Axis 165 with a mono-aluminum gun at 160 eV pass energy for full range scan and 40 eV pass energy for detailed scan. Raman spectra were collected using the Bruker Senterra system (Bruker Optics Inc.). A neon laser with wavelength of 785 nm and power of 10 mW was used. The integral time and co-additions were 15 s and 2, respectively. FTIR spectra were obtained on a Nicolet 4700 FTIR instrument. The UV-vis absorbance spectra were obtained using a DH-2000 UV-VIS-NIR light source. Fluorescence images were captured using the Zeiss Axiovert 200 Inverted Fluorescence Microscopy with an excitation wavelength of ~490 nm. The electrical characterization (I-V test) of the Si substrates patterned with various nanostructures was carried out using a two-point probe micro-manipulator set-up equipped with Keithley source meters.

3. Results and discussion

Scheme 1 (steps a-e) outlines the approach for the patterned growth of GNPs, their surface functionalization, and attachment with quantum dots. This involves the following steps: (a) Deposition of Au film on a Si substrate, (b) high-temperature annealing and dewetting of Au film to result in Au nanoparticles patterned on the Si substrate, (c) CVD growth of multilayer graphene shell on plasma-oxidized Au nanoparticles (patterned GNPs formation), (d) plasma oxidation or acid treatment of patterned GNPs to create carboxylic (-COOH) functionalities

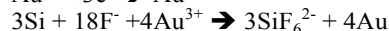
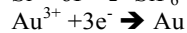
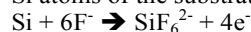
on the multilayer graphene shell, and (e) covalent binding of quantum dots on GNPs to result in the GNP-QD heterostructures. Carbodiimide chemistry (Scheme 1, step e) was used to link -COOH (on GNPs) with -NH₂ (on quantum dots) *via* the formation of amide bonds.²⁵



Scheme 1 Schematic representation of GNP-QD heterostructure fabrication on Si substrate. (a) wet-chemical deposition of Au film, (b) thermal dewetting of Au film to result in patterned Au nanoparticles on the substrate, (c) CVD growth of multilayer graphene shell around Au nanoparticles (patterned GNP growth), (d) wet (acid) or dry (plasma) treatment of patterned GNPs, and (e) covalent functionalization of quantum dots onto GNPs. Note: The covalent chemistry for linking carboxylic (-COOH)-derivatized GNPs with amine (-NH₂)-terminated quantum dots using carbodiimide chemistry is shown for step e in red dotted boxes.

3.1 Synthesis and chemical modification of GNPs

Wet-chemical approach and thermal annealing process were utilized for patterning Au nanoparticles onto the Si substrate. Au film was first deposited onto the Si substrate by treating the latter in a solution of HF and gold salt. This Au film formation is attributed to an electroless mechanism, where Au³⁺ replaces Si atoms of the substrate as follows:³⁷



In the following, The Au film was dewetted at a high temperature (~850 °C) to result in uniform dispersion or patterning of Au nanoparticles (Fig. 1a) on the Si substrate. This approach circumvented the challenges associated with the patterning of metal nanoparticles using chemical and nanofabrication techniques.^{24, 38} The dewetting process is known to involve void/defect formation and vacancy nucleation at the interface of Au film and Si substrate,²⁴ and is responsible for minimal surface energy and stable shape and size of the patterned nanoparticles. Au nanoparticles patterned on the Si substrate were then plasma oxidized to create a surface gold oxide and further utilized for the xylene-based CVD growth of multilayer graphene shell around Au nanoparticles (Fig. 1b).²³⁻²⁵ This approach resulted in uniformly-patterned growth of multilayer graphene shell-encapsulated Au nanoparticles (referred as GNPs) on the Si substrate. The inset in Fig. 1b shows the presence of graphene shell around the Au nanoparticle as compared with the inset in Fig. 1a, which shows the bare as-dewetted Au nanoparticle.

High resolution TEM images indicate (Fig. 1c and d) the multilayer graphene shell encapsulated on the Au nanoparticles. Inter-spacing between the carbon layers in the shell was observed to be $\sim 0.37 \pm 0.02$ nm. This is slightly larger than the c-axis lattice spacing of graphite (~ 0.34 nm) and could be attributed to the curvature structure of the graphene shell.^{23,24,39} The average thickness of the multilayer graphene shell for as-produced GNPs was $\sim 3.8 \pm 0.2$ nm. In addition, it was observed that dewetted Au nanoparticles before CVD growth have an average diameter of $\sim 47.3 \pm 11.3$ nm with an inter-particle spacing of $\sim 49.5 \pm 16.8$ nm on the Si substrate. A minor increase in the average nanoparticle diameter ($\sim 52.2 \pm 11.3$ nm, including shell thickness) and a slight decrease in inter-particle spacing to $\sim 45.1 \pm 13.3$ nm were observed for GNPs after CVD growth (Table S1, see Electronic Supplementary Information, ESI†).

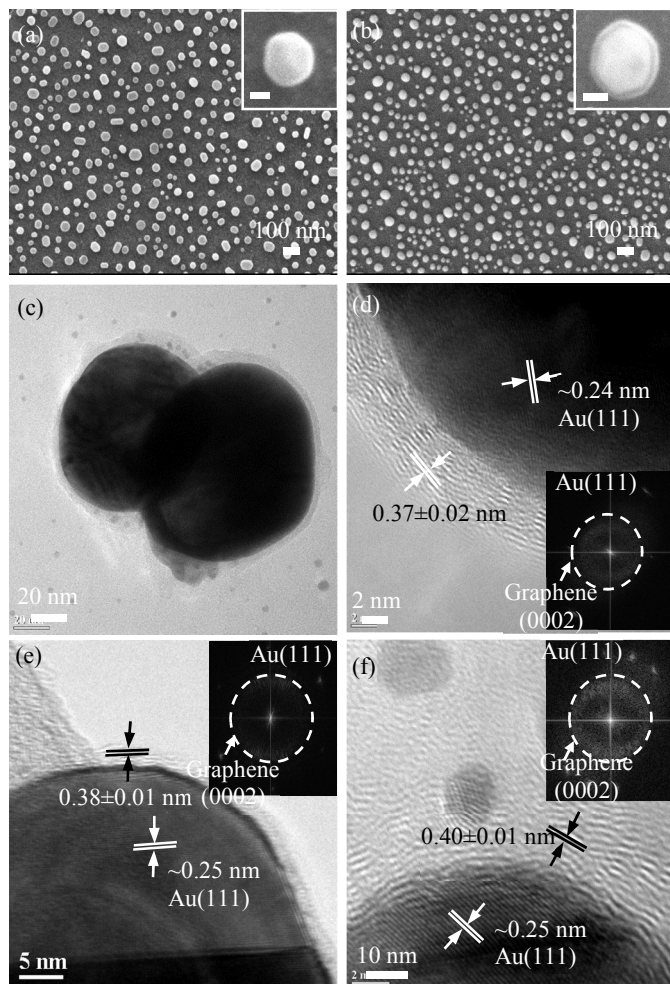


Fig. 1 SEM images for the as-produced and uniformly-patterned Au nanoparticles (a) and GNPs (b). The insets show high-resolution SEM images (scale bar: 25 nm). TEM images of the as-produced GNPs (c and d), GNPs after plasma treatment (e) and acid treatment (f). The insets show corresponding Fast Fourier Transform (FFT) images indicating diffraction of carbon and gold.

Since it was intended to create surface functionalities on GNPs, the substrates with patterned GNPs were treated in acid or oxygen plasma to result in -COOH groups on the multilayer gra-

phene shell. These -COOH groups could facilitate diverse carbon chemistry, which will be of use in modifying surface structure, creating new functionalities, and improving the purity of GNPs.^{25,40,41} Fig. S1a and b (see ESI†) show that GNPs after acid or plasma treatment remained intact and patterned on the Si substrates. As shown in Fig. 1e, plasma oxidation (performed for 10 s) resulted in significant etching of multilayer graphene shell and the shell thickness was decreased to $\sim 0.8 \pm 0.2$ nm. The carbon lattice spacing for plasma-treated GNPs was observed to be $\sim 0.38 \pm 0.02$ nm. The nitric acid treatment had lesser influence on the shell thickness ($\sim 3.4 \pm 0.3$ nm) while lattice spacing increased to $\sim 0.40 \pm 0.01$ nm (Fig. 1f). The minor increase in the carbon lattice spacing after plasma or acid treatment could be attributed to the removal of carbon layers from the shell and the subsequent strain relaxation within the carbon layers.^{23,42}

The variation of nanoparticle density, size, and inter-particle spacing before and after plasma/acid treatment is summarized in Table S1 and Fig. S1c (ESI†). A decrease in GNP diameters observed after the plasma/acid treatment is due to the etching of multilayer graphene shell. Meanwhile, negligible changes in inter-particle spacing were observed. With minor differences in spatial density of nanoparticles on the Si substrate, a decreasing trend was observed as follows: Si substrate patterned with Au nanoparticles > Si substrate patterned with GNPs ~ Si substrate patterned with plasma-treated GNPs > Si substrate patterned with acid-treated GNPs. The CVD growth process involved Ostwald's ripening and Au surface migration,²⁴ and thus resulted in a slight decrease in nanoparticle spatial density as compared to that before CVD growth. Overall, both plasma and acid treatment processes demonstrate a unique approach for surface modification of patterned GNPs and control of the shell thickness. In this regard, the plasma treatment is preferred because of its dry and non-corrosive features for functionalization or controlled etching of the multilayer graphene shell.

Raman spectra of the as-produced GNPs (Fig. 2a, Table S2, ESI†) showed the well-defined G band at ~ 1595 cm^{-1} and D band at ~ 1310 cm^{-1} .^{23,24} The D band in GNPs was observed due to the curvature-induced disorder in the multilayer graphene shell and the existence of amorphous carbon while the G band is a significant indicative of the sp^2 hybridized carbon atoms from the graphitized structure.⁴³ Overall, the peak location of G band for treated or untreated GNPs was different from that for the flat graphene (~ 1580 cm^{-1}). Such shifts in Raman peaks have been attributed to strains in the multilayer graphene shell lattice, shell thickness, and the size of GNPs.²⁴ The acid or plasma treatment of GNPs resulted in a red shift of the G band and D band. The estimated intensity ratio of the D band and G band (I_D/I_G) changed from $\sim 1.34 \pm 0.21$ to $\sim 1.25 \pm 0.30$ after acid treatment due to the purification of GNPs. On the other hand, the plasma treatment significantly decreased the intensity of the D band and G band, indicating this process was more rigorous than acid purification.⁴⁴ This observation was also proved by the TEM result (Fig. 1e). The estimated I_D/I_G ratio for plasma-treated GNPs was $\sim 1.75 \pm 0.25$, which indicates that this process led to more defects and disordered structure within the multilayer graphene shell.

To better understand the plasma/acid treatment process, XPS studies were performed for Au nanoparticles, surface oxidized Au nanoparticles, and GNPs (before and after acid/plasma treatment).^{23,45} XPS survey scans (Fig. S2, Table S3, ESI†) ranging between 0 eV and 1000 eV indicated the presence of various elements such as Au, C, O, and Si. The Si peaks arise due to the substrate. For O 1s peaks, there could be several ori-

gins, such as adsorbed molecules and native oxide (SiO_2) from the substrate.²³ So, O 1s peaks should not be utilized for analyzing plasma oxidized Au nanoparticles and surface-modified GNPs. For the as-prepared Au nanoparticles, pure element Au peaks consistent with Au $4f_{7/2}$ and Au $4f_{5/2}$ were observed at ~ 84.59 eV and ~ 88.27 eV, respectively (Fig. S3a, ESI[†]).²³ After the plasma oxidation of Au nanoparticles (Fig. S3b, ESI[†]), two new and additional peaks corresponding to surface gold

oxide at ~ 85.34 eV and ~ 88.90 eV emerged.²³ These two additional peaks disappeared after the GNP growth (Fig. S3c, ESI[†]) but re-emerged after the plasma treatment (Fig. S3d, ESI[†]). However, these two oxide peaks were not observed after the acid treatment (Fig. S3e, ESI[†]). This further confirmed the rigourosity of the plasma treatment process, which must have partially exposed some Au nanoparticles (see Fig. 1e) and surface oxidized them.

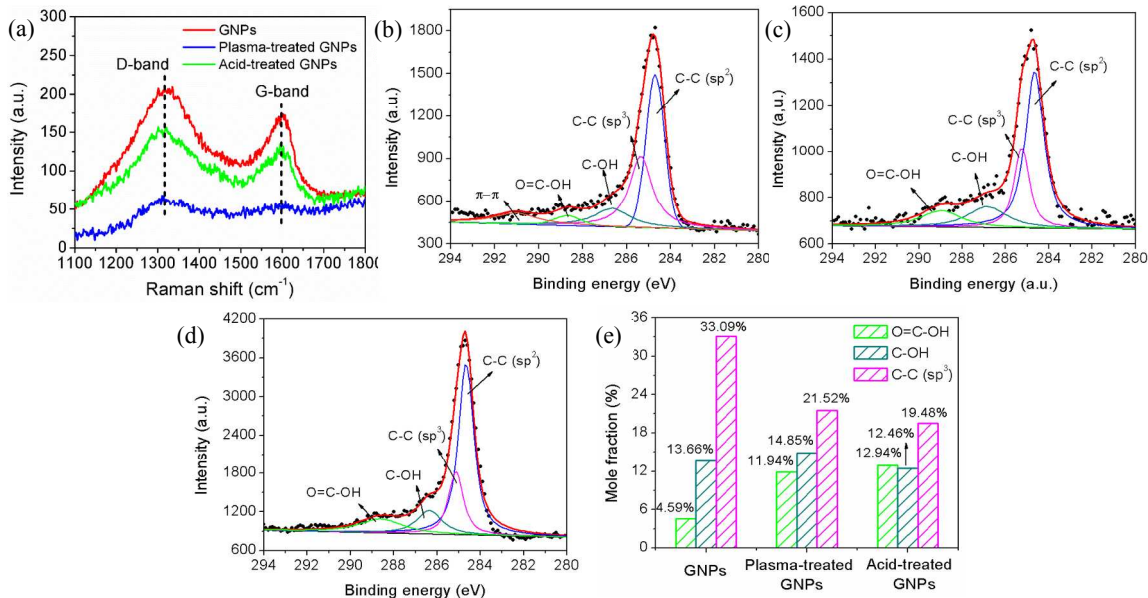


Fig. 2 (a) Raman spectra of the as-produced GNPs, GNPs after plasma or acid treatment. (b-d) Deconvoluted XPS spectra (C 1s) for (b) as-produced GNPs and GNPs after (c) plasma and (d) acid treatment. (e) Mole fraction of -COH, -COOH, and C-C for GNPs before and after plasma/acid treatment estimated using C 1s peaks. *NOTE: The scatters (black dots) in (b-d) show the XPS results and the solid lines show the fitted data.*

XPS C 1s peak was evaluated for the as-produced GNPs as well as GNPs after plasma or acid treatment (Fig. 2b-d). This peak is asymmetric with long tail extending to the higher energy region and has been explained in terms of the metallic conduction electron interactions induced by low energy electron-hole excitations resulting from the absorption of X-rays.⁴⁵ Further deconvolution of C 1s peak showed five Gaussian peaks centered at $\sim 284.7 \pm 0.1$ eV (C-C in sp²), $\sim 285.2 \pm 0.2$ eV (C-C in sp³), 286.6 ± 0.2 eV (-COH), 288.7 ± 0.2 eV (-COOH), and 291.2 eV ($\pi-\pi^*$ transition loss peak). The peak at ~ 291.2 eV corresponds to the electron energy loss peak due to the π -plasmon excitations. The delocalized π -conjunctions are attributed to graphene and also reported to disappear with increasing oxidation.⁴⁶ This phenomenon was also observed for GNPs after acid or plasma treatment in this study (Fig. 2c and d). Moreover, electronegative oxygen atoms induce positive charges to carbon atoms, thus peaks with high binding energies located at ~ 286.6 eV and ~ 288.7 eV are considered to originate from carbon-oxygen links, corresponding to -COH and -COOH groups, respectively.⁴⁵ The peak at ~ 285.2 eV was attributed to the photoelectrons emitted from the diamond-like carbon atoms hybridized *via* the sp³ bond. This has been reported as evidence for the presence of amorphous carbon resulting from the CVD growth of carbon materials.⁴⁷ Meanwhile, the peak at ~ 284.7 eV is associated with the hexagonal carbon atoms in sp² hybridization. As a result, the area ratio of C-C sp² and sp³ peaks is an indicative of degrees of graphitization.

Fig. 2e shows the percentages of various functional groups (-COH, -COOH, and sp³ hybridized C-C) estimated using the deconvoluted C 1s spectra for GNPs before and after plasma or acid treatment. The presence of carbon-oxygen groups (-COOH and -COH) before treatment of GNPs could be attributed to the absorption of water vapor and the contamination due to air exposure.⁴⁸ The content of sp³ C-C bonds was considerably decreased after the plasma and acid treatment, indicating both approaches improved the quality of graphitic carbon in GNPs,⁴⁸ which further supports the microscopic and Raman spectroscopy results (Fig. 1d-f and Fig. 2a). Moreover, negligible changes in -COH groups were observed before and after the plasma or acid treatment of GNPs. However, the -COOH groups percentage increased from $\sim 4.5\%$, for the as-produced GNPs, to 11%-12% after plasma or acid treatment. It must be noted that -COOH groups were most critical for further chemical functionalization of GNPs. Overall, a 15 s plasma oxidation of GNPs was much more rigorous and controlled as compared to the 5 h acid treatment. In addition, the former provides a dry processing route and results in thinner multilayer graphene shell (< 1 nm).

3.2 Fabrication of GNP-QD heterostructures

Chemical functionalization of GNPs with surface -COOH groups facilitated their combination with (-NH₂)-terminated QD

(referred as GNP-QD heterostructures) by using the well-established carbodiimide linking chemistry (Scheme 1). This process mainly involves the formation of covalent amide bonds between GNPs and quantum dots, as illustrated in Fig. 3a.^{5,25,49} Both, acid- and plasma-treated GNPs were utilized for fabricating GNP-QD heterostructures. FTIR was used to study the surface functional groups for various samples including (1) as-produced GNPs, (2) acid-treated GNPs, (3) plasma-treated GNPs, (4) acid-treated GNPs linked with quantum dots, and (5) plasma-treated GNPs linked with quantum dots (Fig. 3b, Table S4, ESI†). Spectra for all these samples (Fig. 3b) shows broad peaks within 1510-1540 cm^{-1} , which is corresponding to the stretching of C-C bonds and/or C-H bonds on multilayer graphene shell.⁵ Peaks for -COH stretch was observed at ~ 1450

cm^{-1} for all the samples. Meanwhile C=O stretches originated from the surface carboxylic groups were observed at $\sim 1690 \text{ cm}^{-1}$ after plasma or acid treatment.⁵⁰ These observations show a good consistence with the XPS results in Fig. 2e. Further, after carbodiimide-based linking of quantum dots on GNPs, FTIR spectra show the emergence of amide I, II, and III peaks (Fig. 3a) at $1650\text{--}1670 \text{ cm}^{-1}$, $1550\text{--}1570 \text{ cm}^{-1}$, and $1230\text{--}1240 \text{ cm}^{-1}$.⁵¹ This further confirms the presence of covalent amide bonds (-CONH-) between the (-NH₂)-terminated quantum dots and (-COOH)-terminated GNPs. Amide I band appeared around $\sim 1660 \text{ cm}^{-1}$ was assigned to the C=O stretch. Amide II and III bands appeared at 1550 cm^{-1} and 1240 cm^{-1} were attributed to the stretching of C-N and/or blending of N-H, respectively.⁵¹

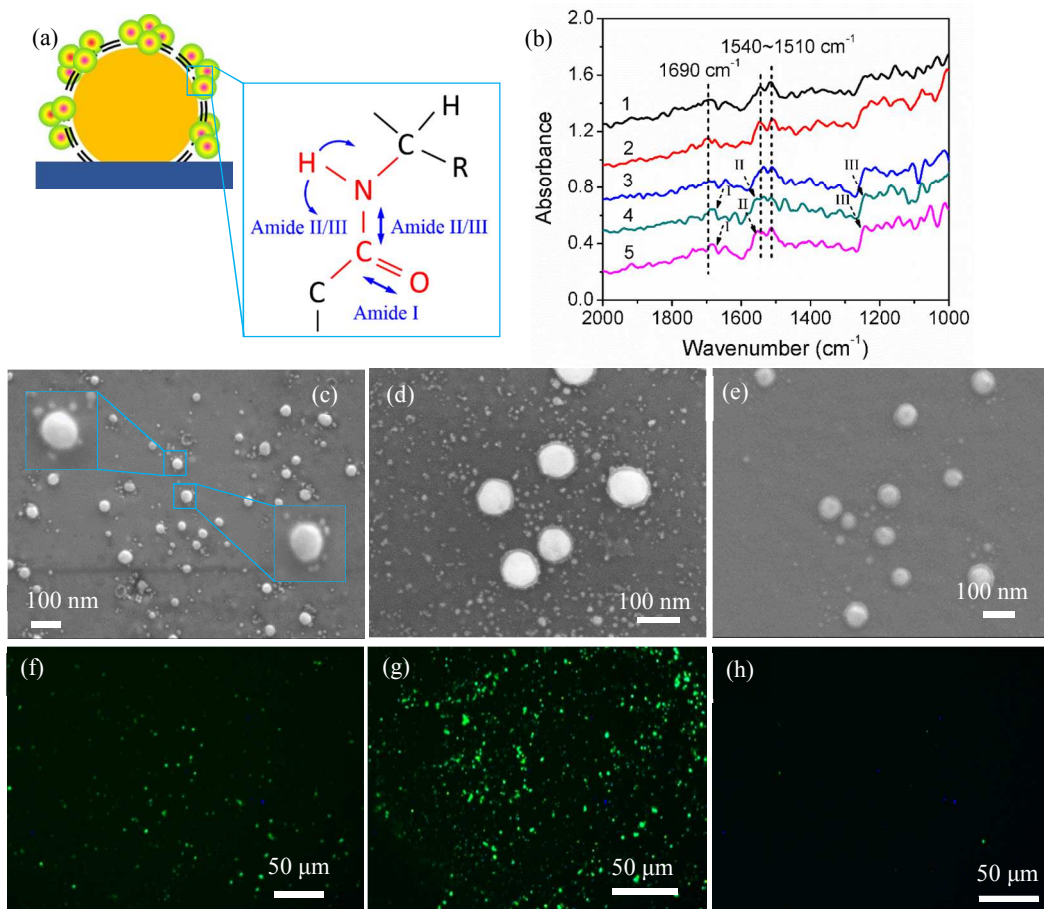


Fig. 3 (a) Schematic of the GNP-QD heterostructures and the necessary amide bonds formed between GNPs and quantum dots. (b) FTIR spectra of (1) as-produced GNPs, (2) GNPs after plasma treatment, (3) GNPs after acid treatment, (4) GNP(plasma-treated)-QD heterostructures, and (5) GNP(acid-treated)-QD heterostructures. SEM images of the GNP-QD heterostructures fabricated using (c) plasma- and (d) acid- treated GNPs. (e) Control sample that used as-produced GNPs with no -COOH surface derivatization for physically binding with quantum dots. (d-f) Fluorescence images corresponding to samples (c-e).

The approach of functionalizing GNPs and linking with quantum dots was achieved directly on the Si substrate and the processes resulted in patterned GNP-QD heterostructures (Fig. 3c-e). Prior to microscopic evaluations, substrates were washed with DI-water to remove non-specifically bound or physically-adsorbed quantum dots. Although difficult to differentiate, a careful examination of SEM images shows small aggregated dots around plasma- or acid-treated GNPs (Fig. 3c and d). This

was not observed for the as-produced GNPs that only immersed in a quantum dots solution but without processing the carbodiimide chemistry (Fig. 3e), suggesting that surface -COOH groups on GNPs and carbodiimide-based linkages were critical for fabricating GNP-QD heterostructures. These observations were supported by fluorescence microscopy of the respective samples, where quantum dots were observed as green dots (excitation $\lambda \sim 365 \text{ nm}$ and emission $\lambda \sim 490 \text{ nm}$, Fig. 3f and g),

which were absent in the case of the as-produced GNPs with no functional chemistry (Fig. 3h). In other words, functional chemistry on patterned GNPs not only provides a unique route to assemble quantum dots but also is proved to be a selective tagging approach.

High resolution TEM images (Fig. 4a-c) demonstrate GNPs coated with quantum dots (diameter ~ 4 nm, lattice spacing ~ 0.35 nm). Pristine quantum dots showed similar size and lattice spacing (Fig. S4, ESI[†]), which helped in differentiating quantum dots from GNPs in the TEM analysis (Fig. 4). Approximately, $\sim 22\%$ of the GNP surface was covered with quantum dots. Electron diffraction, EDS spectra, and scanning transmission electron microscopy (STEM)-mode line profile showed the crystal structure, chemical composition, or elements present in the GNP-QD heterostructures (Fig. 4d-g). This provides another strong evidence for the effective linking of quantum dots on the surface of GNPs and, at the same time, indicates that GNPs and quantum dots were structurally and chemically intact in the heterostructures. To further confirm this EDS elemental study, XPS analysis of the quantum dots and GNP-QD heterostructures (Fig. S5 and S6, ESI[†]) was conducted. Fig. S5 shows the XPS survey scans of the pristine quantum dots

and the covalently-linked GNP-QD heterostructures. Different elements such as Cd, Zn, S, O, C, and Au were observed.⁵² Deconvoluted spectra for Cd, Se, Zn and S for the quantum dots were evaluated (Fig. S6, see ESI[†]). Cd peaks consistent with Cd 3d_{3/2} and Cd 3d_{5/2} were observed at ~ 412.78 eV and ~ 406.07 eV, respectively. These were slightly shifted from ~ 405.0 eV and ~ 411.7 eV of the standard peak of pure Cd element due to the sulfuration (formation of CdS).⁵² Similarly, Zn peaks corresponding to Zn 2p_{1/2} and Zn 2p_{3/2} were observed at ~ 1045.76 eV and ~ 1022.52 eV, which were also shifted from standard peaks of pure Zn (~ 1044.8 eV and ~ 1021.8 eV) due to the sulfuration. For S peaks, S 2p_{1/2} and S 2p_{3/2} were observed at 163.94 eV and 162.75 eV. These values were also shifted from standard S peaks (~ 165.1 and ~ 163.9).⁵² No obvious peaks (dotted line, Fig. S5b, ESI[†]) were observed for Se or were not detected due to instrumental limitations. This suggests that Se content in the quantum dots was negligible and the configuration can be recognized as CdS/ZnS structure. It also needs to mention that insignificant shifts were observed for peaks corresponding to quantum dots after their covalent binding with GNPs, which further confirms that all the components in the heterostructures remains chemically intact.

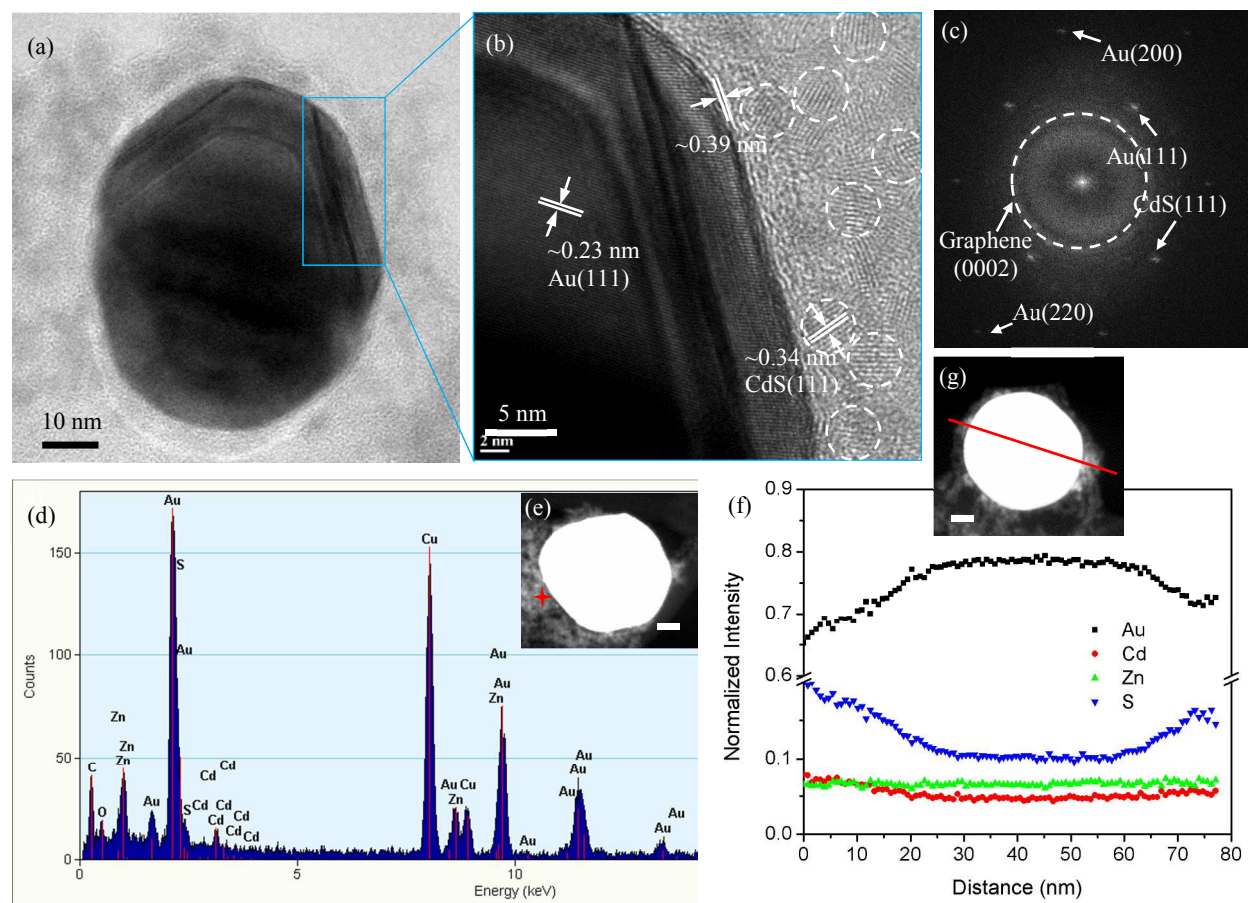


Fig. 4 (a, b) TEM images of the GNP-QD heterostructures formed on the plasma-treated GNPs. (c) FFT image corresponding to (b). (d and e) Representative STEM mode spot EDS analysis and (f and g) STEM mode EDS line profile analysis of the GNP-QD heterostructures. *Note: The dotted circles in (b) indicate quantum dots and the red spot and line in (e) and (g), respectively, shows the analysis spot and line for EDS profiling.*

3.3 Optical properties of GNPs and GNP-QD heterostructures

UV-vis absorbance spectra (Fig. 5a, Table S5, see ESI†) for Au nanoparticles, GNPs, and GNPs after plasma or acid treatment were studied. The inset in Fig. 5a shows the sample dispersions in DI-water. Bare Au nanoparticles resulted in a characteristic visible absorption peak with 500-650 nm. After the GNP formation and their acid or plasma treatment, absorbance peaks centered at ~280-293 nm and ~500-650 nm were observed. The former peak is associated with the presence of multilayer graphene shell and attributed to the π - π^* transition of electrons in the aromatic double bonds.^{26,53} The latter peak (~500-650 nm) is due to the encapsulated Au nanoparticles. The shift of such broad peak is hard to comment but overall no significant shift can be estimated after the multilayer graphene shell encapsulation or after the acid or plasma treatment (Table S5, ESI†). Thus, one can understand that the presence of multilayer graphene shell around Au nanoparticles and their further acid/plasma treatment did not suppress the optical properties (e.g. surface plasmon resonance) of the latter, which is consistent with the simulated absorption spectra for GNPs with approximately similar size and shell thickness.²⁶

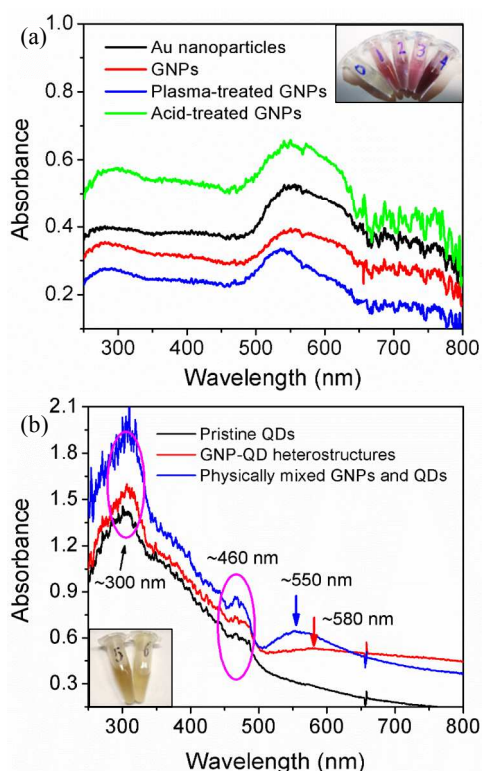


Fig. 5 (a) UV-vis spectra for Au nanoparticles, as-produced GNPs, and GNPs after plasma and acid treatment. (b) UV-vis spectra of pristine quantum dots, GNP-QD heterostructures, and physically mixed GNPs and quantum dots. *Note:* The insets showing digital images of dispersed (1) pristine quantum dots, (1) Au nanoparticles, (2) as-produced GNPs, (3) plasma-treated GNPs, (4) acid-treated GNPs, (5) physically mixed GNPs with quantum dots, and (6) GNP-QD heterostructures.

Plasma-treated GNPs were utilized for fabricating GNP-QD heterostructures and the UV-vis spectra of the latter (Fig. 5b) shows broadened and red-shifted Au absorption peak (~580

nm) and graphene absorbance peak (~305 nm) with respect to the plasma-treated GNPs. This could be attributed to the attachment of quantum dots, which enhanced the absorbance spectrum of GNPs and lowered the absorbed energy.⁵⁴ The peak corresponding to quantum dots was observed at ~460 nm and remained unchanged from that of the pristine quantum dots.⁵⁵ In addition, a control sample was studied for absorbance peaks, where quantum dots were physically mixed with plasma-treated GNPs. For this control sample the Au absorption peak was remaining at ~500-650 nm and no significant shift was observed with respect to the plasma-treated GNPs. Digital images for these samples were also put as inset for further confirmation. This absorption property study indicates that only covalently linked quantum dots have a strong interaction with Au nanoparticles when covalently linked with GNPs, where multilayer graphene shell acted as a unique interface between Au nanoparticles and quantum dots.

Previous simulation studies have shown that the resonance peak of Au nanoparticle encapsulated within multilayer graphene shell varies within a broad range (~527-663 nm) according to the size and shell thickness of GNPs.²⁶ And the scattering component of the extinction efficiency spectra was negligible for the small-sized GNPs (< 50 nm)²⁶ In this study, the optical properties of Au nanoparticles, GNPs (before and after plasma treatment), and the GNP-QD heterostructures were further simulated and compared using the Discrete Dipole Approximation (DDA) method. These targets were comprised of an arrangement of dipoles for which extinction spectra and normalized electric field distributions were numerically solved. It is important to mention here that the quantum dot target was only comprised of CdS/ZnS core/shell structure as Se content was negligible as indicated in Fig. S5 and S6 (see ESI†). UV-vis reflectance and absorbance spectra were collected for the pristine quantum dots (Fig. S7, ESI†) and further utilized to estimate effective refractive index (real and imaginary components)⁵⁶ for the quantum dots. The spherical targets (Fig. 6a-h) were derived by considering experimental Au nanoparticle size (~50 nm), multilayer graphene shell thickness (~3.8 nm for as-produced GNPs or 0.8 nm for plasma-oxidized GNPs), and size of quantum dots (~4 nm). Quantum dots were assumed to be closely-packed around the GNPs (Fig. 6d and h). The surrounding environment was set as water, which is nearly consistent with the experimental UV-vis spectroscopy study (Fig. 5).

The extinction efficiency is given by a combination of scattering and absorption components as follows:

$$Q_{ext} = Q_{sca} + Q_{abs}, \quad (2)$$

where Q_{ext} is the extinction efficiency factor, Q_{sca} is the scattering efficiency factor and Q_{abs} is the absorbance factor. The extinction spectra (Fig. 6i) were deconvoluted into absorbance and scattering spectra (Fig. S8, ESI†). DDA calculations for bare Au nanoparticles resulted in extinction efficiency peak at ~538 nm.⁵⁷ Another peak in the UV region (~270 nm) was observed for bare Au nanoparticles and could be attributed to the interband transition because of the excitation of d electrons.^{57,58} This peak was significantly suppressed for experimental absorbance (Fig. 5a) probably due to the difference in dielectric environment in experiment and simulation, where the latter presented an ideal environment. For the as-produced GNPs with a shell thickness of ~3.8 nm, insignificant suppression of Au absorption peak (~562 nm) was observed but this peak was red-shifted with respect to the bare Au nanoparticles. The red shift is attributed to the presence of graphene shell. This observation is hard to comment on the experimental UV-vis spectra

(Fig. 5a) due to the broad peak feature. After plasma treatment, this peak shifted back to ~ 540 nm due to the etching of graphene shell. Moreover, The Au absorption peak of GNP-QD heterostructures show minor intensity increase and slight red-shift (~ 543 nm) with respect to bare Au nanoparticle, indicating the light-matter interaction happened between Au nanoparticle, graphene shell and the attached quantum dots.

For all the targets simulated here, the scattering component was significantly suppressed as compared to the absorption component (Fig. S8, ESI†). This is due to the defect-free target structure and their significantly smaller size relative to incident wavelength.⁵⁹ As reported earlier,⁶⁰ when nanoparticles are much smaller compared to the wavelength of incident light, the scattering is in the Rayleigh regime. In that case, the scattering (Q_{sca}) can be written as:

$$Q_{sca} = \frac{8\pi}{3} k^4 R^6 F(m) \quad (3)$$

where $k = \frac{2\pi}{\lambda}$ (λ is the wavelength), R is the radius of the particles, and $F(m)$ is a function of the refractive index (m). The absorption (Q_{abs}) can be written as:

$$Q_{abs} = 4\pi k R^3 E(m) \quad (4)$$

where $E(m)$ is also the function of the refractive index relying on a non-zero imaginary part. Thus, the ratio of scattering to absorbance is $\frac{2}{3} (kR)^3 \frac{F}{E}$, which is further equivalent to $(kR)^3$. In this simulation, the average diameter of the heterostructures is ~ 50 nm ($R = 25$ nm). And considering an incident wavelength of ~ 500 nm, the ratio is: $(kR)^3 = 0.03$. This result demonstrates a good agreement with the ratio of scattering to absorbance observed in Fig. S8 (see ESI†).

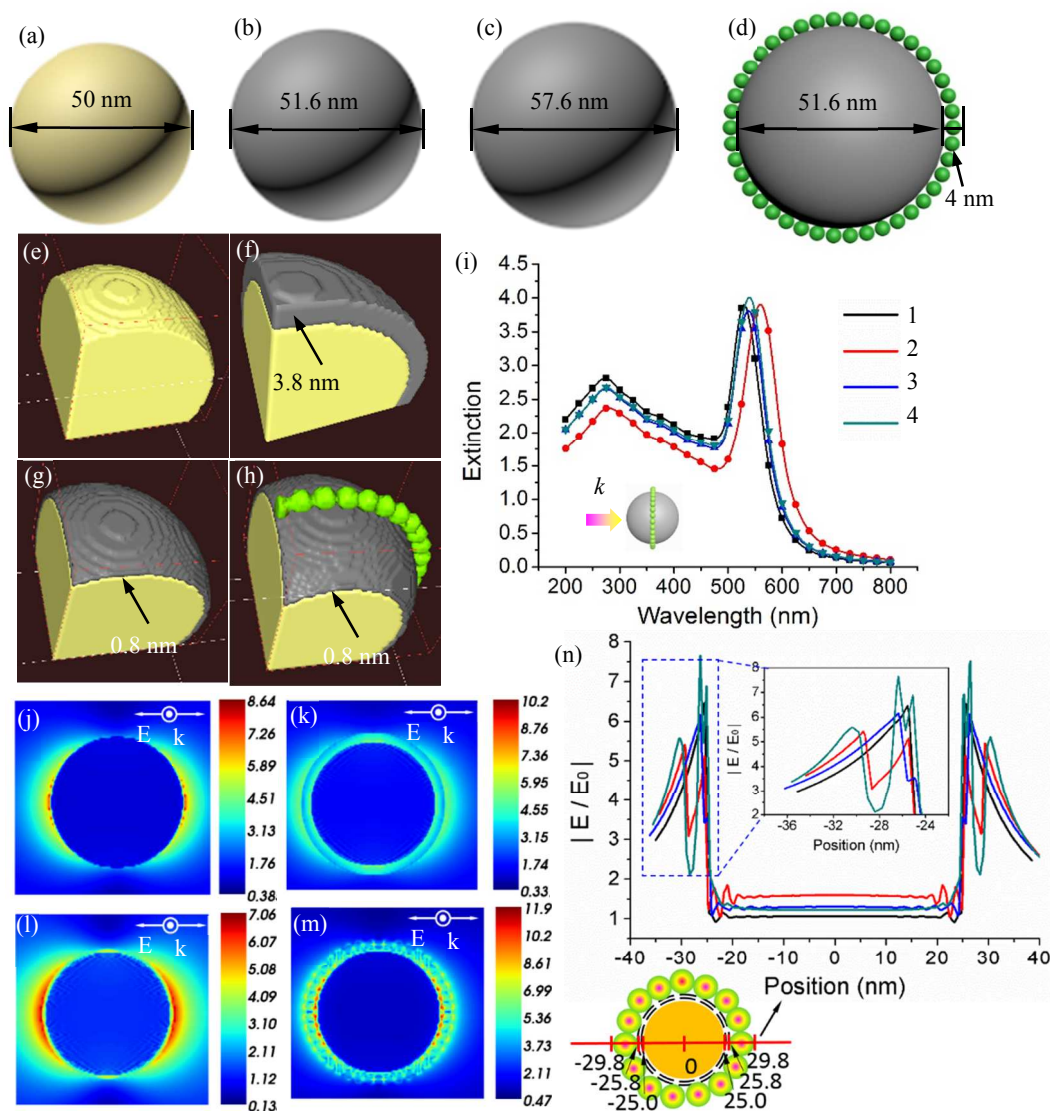


Fig. 6 Targets: (a, e) Au nanoparticle, (b, f) GNP, (c, g) plasma-treated GNP, and (d, h) GNP-QD heterostructure. (i) Simulated extinction spectra for Au nanoparticles (1), GNPs (2), plasma-treated GNPs (3) and GNP-QD heterostructures (4). (j-m) Normalized electrical field distribution ($|E/E_0|$) near the surface of (j) Au nanoparticle (incident wavelength ~ 538 nm), (k) as-produced GNPs (shell thickness ~ 3.8 nm, incident wavelength ~ 562 nm), (l) plasma-treated GNPs (shell thickness ~ 0.8 nm, incident wavelength ~ 540 nm), and (m) GNP-QD heterostructure (incident wavelength ~ 543 nm). (n) $|E/E_0|$ vs. position along the center of the targets across the incident direction for target 1-4 in (i). Note: Schematic in (i) shows the target and incident wavevector (k). Schematic in (n) shows ideal GNP-QD heterostructure and various positions plotted in (n).

3.4 Photocatalytic degradation of phenol

Tauc plots (Fig. 7a) were generated from the UV-vis absorbance spectra (Fig. 5b) to estimate the band gap energies of the pristine quantum dots, GNP-QD heterostructures, and physically-mixed GNP-QD. For all these three samples, band gap energies of ~ 3.4 eV and ~ 2.6 eV were estimated corresponding to ZnS and CdS, respectively, present in the quantum dots.⁶¹ A band gap tail corresponding to ~ 1.5 eV was also observed for the samples due to quantum confinement effects. Since all the samples including pristine quantum dots shows same band gap energies, the photoactivity of GNP-QD heterostructures is dominated by these attached semiconducting quantum dots. This further indicates that GNPs have metallic character, which was confirmed by the electrical characterization in Fig. 7b. The inset digital image shows the device for I-V test. Embedded I-V curves in Fig. 7b indicate that the blank Si substrate has semiconducting behavior and a rectifying diode effect was observed with a turn-on voltage of ~ 0.25 V.⁶² The metallic characteristics (conducting) emerged after the Au nanoparticles patterning. The remaining rectification effect on this Au nanoparticle-patterned substrate was due to the Schottky barrier between the Au and Si.⁶² On further growth of GNPs, almost linear I-V relationship was observed and the estimated resistance is ~ 16790 Ω . For the GNP-QD heterostructure patterned substrate, the estimated resistance increased to ~ 70040 Ω and this loss of metallic character was observed with respect to GNPs due to the low conductivity of quantum dots.

Above band gap and electric characterizations are of use in understanding the photocatalytic behaviors of the GNP-QD heterostructures. In this regard, photodegradation of phenol was studied with the absence or presence of various photocatalysts including the pristine quantum dots, the as-produced GNPs as well as the GNP-QD heterostructures. As shown in Fig. 7c, the GNP-QD heterostructures showed the best photocatalytic efficiency ($\sim 40\%$) within 2 h of degradation reaction. The other samples demonstrated the following order of photodegradation efficiencies: GNPs (26%) > pristine quantum dots (17%) > without any photocatalyst (12%). The degradation without any photocatalyst could be attributed to the presence of sacrificial agent and UV-based self-degradation of phenol.⁶³ The activity of GNPs could be due to the heterogeneous catalysis and their improved electrical conductivity (Fig. 7b). Pristine quantum dots show lower photodegradation efficiency than GNPs because of their natural narrow band gap energy, which resulted in significant self-recombination of the excited electrons.⁶⁴ The Photodegradation efficiency was improved after 2 h for all the systems. This is probably due to the increase of solution temperature during long time optical heating.⁶⁵ However, at this period, lower photocatalytic efficiency was observed for the GNP-QD heterostructures as compared with the pristine quantum dots and GNPs. This is probably due to the decomposition of quantum dots in the presence H_2O_2 and GNPs under UV illumination.^{66,67} H_2O_2 is a strong oxidizing agent for both CdS and ZnS⁶⁶ while GNPs provide numerous heterogeneous catalysis sites for the decomposition reaction⁶⁷.

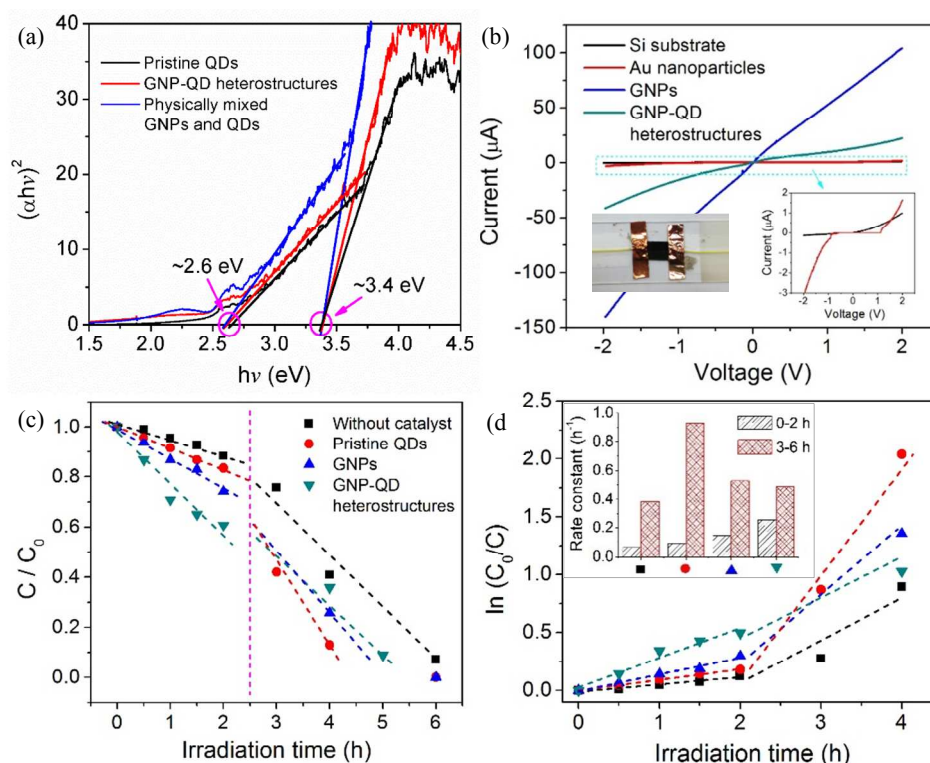


Fig. 7 (a) Tauc plots obtained from the UV-vis spectra (Fig. 5b) indicating band gap energies and tailings for various samples. (b) I-V curves for various samples (all samples were on the Si substrate). The inset DC image shows the digital image of the device. (c) Experimental photodegradation of phenol under UV irradiation (8 W lamp) in presence of sacrificial agent (H_2O_2) and different samples as photocatalyst. (d) First order fit of various phenol degradation processes indicated in (C). Note: The legend in (d) is as shown in (c).

To further study the photodegradation kinetics, the first order rate constant (k) was estimated using the following kinetic equation:³⁶

$$k = \frac{1}{t} \ln \frac{C_0}{C} \quad (5)$$

where t is the degradation time, C_0 is the initial phenol concentration in water and C is the phenol concentration at specific t . As shown in Fig. 7d, the plots of $\ln(C_0/C)$ vs. time show good linear trend for these photodegradation processes, which allows for the estimation of their apparent first order kinetic constant (showing as inset in Fig. 7d). The photodegradation in 3-6 h exhibited obviously increased rate constant. However, since the quantum dots were partially decomposed as we described above, the rate constant in the first 2 h is a real indication of the photocatalytic activity of the GNP-QD heterostructures. In 0-2 h, photodegradation in the presence of pristine quantum dots shows a rate constant of 0.092 h^{-1} , which is comparable with the values reported in previous studies.⁶⁸ The GNP photodegradation shows increased rate constant of 0.144 h^{-1} while the photodegradation with GNP-QD heterostructures shows the highest (0.257 h^{-1}). This rate constant value is much higher as compared with that reported in similar photocatalysis processes using semiconducting quantum dots⁶⁸ or metal oxide nanostructures,³⁶ indicating such GNP-QD heterostructures can be a preferred photodegradation catalyst. The band diagram and charge transfer on GNP-QD heterostructures was further proposed in Fig. 8. Graphene shell and Au nanoparticle present lower band energy⁶⁹ than the conduction bands of CdS and ZnS, which facilitated the transfer of excited electron from quantum dots to GNPs. We can predict according to previous literatures⁶¹ that charge transfer process resulted in more holes on the valence band for the oxidation of phenol and meanwhile accumulated more electrons on GNPs for the decomposition of H_2O_2 , which provided $\text{OH}\cdot$ radicals for the phenol oxidation. This is probably the reason for the high photocatalytic activity of the GNP-QD heterostructures.

In addition, it is worthy to mention that the GNP-QD heterostructures exhibit strong plasmonic effect as proved by above DDSCAT modeling, which indicates that such heterostructures can be used for the plasmon-enhanced photocatalysis. Since the strongest plasmonic effect was observed in 500-600 nm, it is reasonable to predict that the GNP-QD heterostructures can be used in visible or solar driven photocatalysis processes. Meanwhile, visible or solar light with low energy has less damage to the quantum dots, which makes it possible to achieve long-term photocatalysis.

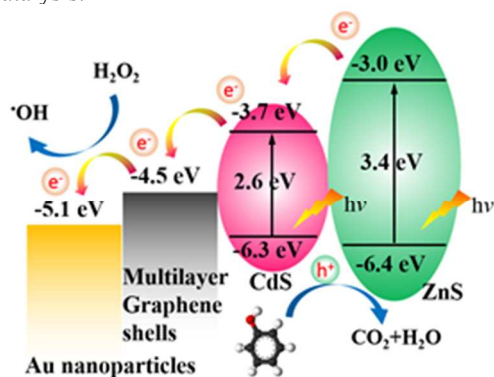


Fig. 8 Band gap energy and relative band edge locations for GNP-QD heterostructures. The electron transfer as well as degradation reaction under illumination are indicated by arrows.

Conclusions

For the first time we report the patterned growth of GNPs in a facile CVD approach and their hybridization with semiconducting quantum dots directly on a Si substrate. Sequential steps for the heterostructure synthesis involved the electroless deposition of Au film, high-temperature annealing (to form Au nanoparticles), CVD growth of multilayer graphene shell around the Au nanoparticles, and covalent binding of quantum dots on GNPs. The surface functionalization of GNPs was achieved through both plasma and acid treatment and this processing had no significant impact on the distribution of GNPs on the substrate. XPS analysis of plasma- or acid-treated GNPs indicated that both processes were able to create carboxylic ($-\text{COOH}$) groups ($\sim 12\%$ *via* plasma treatment and $\sim 13\%$ *via* acid treatment) on the surface of GNPs, which facilitated the covalent linking of ($-\text{NH}_2$)-terminated semiconducting quantum dots. The covalent linking was achieved *via* carbodiimide chemistry, resulting in the formation of amide bond as confirmed by FITR. Optical studies, both experimental and simulated, indicated that the encapsulation of multilayer graphene shell around Au nanoparticles did not suppress the extinction/plasmonic characteristics of the latter. The simulation of optical behavior of GNP-QD heterostructures showed intense “hot spots” at the interface of GNP and quantum dots. Band gap and electrical characterization indicated that the heterostructuring process has minimal influence on the band gap energies of quantum dots and meanwhile the GNPs exhibited strong metallic behavior. Thus, GNP-QD heterostructures were further employed for the photocatalytic phenol degradation. The results indicate that the GNP-QD heterostructures exhibited the highest degradation efficiency ($\sim 40\%$) or rate constant (0.257 h^{-1}) as compared with the pristine quantum dots or GNPs.

Acknowledgements

This work was supported by National Science Foundation (Award #: 0925445) and NSF-EPSCoR-R11 award. The authors thank the University of Alabama’s Office of sponsored programs and Research Grant Committee Award for additional support for this research. The authors thank the Central Analytical Facility (CAF). The research project was conceptualized and planned by N. C while Y. L. helped with data collection. The authors thank Dr. S. Kapoor for proof reading the manuscript.

Notes and references

^a Metallurgical and Materials Engineering Department, Center for Materials for Information Technology (MINT), The University of Alabama, Tuscaloosa, AL 35487, U.S.A.

^b Department of Biological Sciences, The University of Alabama, Tuscaloosa, AL 35487, U.S.A.

^c Department of Chemistry, The University of Alabama, Tuscaloosa, AL 35487, U.S.A.

* nchopra@eng.ua.edu; Tel: 205-348-4153

Electronic Supplementary Information (ESI) available: [Tabulated data for size, inter-particle spacing, nanoparticle spatial density, Raman, XPS, FT-IR, UV-vis peaks; SEM images of GNPs after plasma/acid treatment;

TEM image of quantum dots and GNP-QD heterostructures; XPS survey scan and spectra for Au 4f and quantum dots; Experimental absorbance and reflectance for quantum dots]. See DOI: 10.1039/b000000x/

References

- 1 A. Kudo and Y. Miseki, *Chem. Soc. Rev.*, 2009, **38**, 253-278.
- 2 M. N. Chong, B. Jin, C. W. Chow and C. Saint, *Water res.*, 2010, **44**, 2997-3027.
- 3 S. SanthosháBabu, *J. Mater. Chem.*, 2012, **22**, 22370-22373.
- 4 R. Asahi, T. Morikawa, T. Ohwaki, K. Aoki and Y. Taga, *Science*, 2001, **293**, 269-271.
- 5 D. E. Macphee, D. Rosenberg, M. G. Skellern, R. P. Wells, J. A. Duffy, K. S. J. Killham, *Solid State Electrochem.*, 2011, **15**, 99-103.
- 6 I. Robel, V. Subramanian, M. Kuno and P. V. Kamat, *J. Am. Chem. Soc.*, 2006, **128**, 2385-2393.
- 7 R. S. Selinsky, Q. Ding, M. S. Faber and S. Jin, *Chem. Soc. Rev.*, 2013, **42**, 2963-2985.
- 8 W. Hou and S. B. Cronin, *Adv. Func. Mater.*, 2013, **23**, 1612-1619.
- 9 Z. Zhang, Z. Wang, S. W. Cao and C. Xue, *J. Phys. Chem. C*, 2013, **117**, 25939-25947.
- 10 T. Ribeiro, T. J. V. Prazeres and J. P. S. Farinha, *J. Phys. Chem. C*, 2013, **117**, 3122-3133.
- 11 O. Kulakovich, N. Strekal, A. Yaroshevich, S. Maskevich, S. Gaponenko, I. Nabiev and M. Artemyev, *Nano Lett.*, 2002, **2**, 1449-1452.
- 12 X. Peng, J. Chen, J. A. Misewich and S. S. Wong, *Chem. Soc. Rev.*, 2009, **38**, 1076-1098.
- 13 J. H. Bang and P. V. Kamat, *ACS nano*, 2011, **5**, 9421-9427.
- 14 N. Chopra, M. Majumder and B. J. Hinds, *Adv. Funct. Mater.*, 2005, **15**, 858-864.
- 15 A. Mondal and N. R. Jana, *ACS Catal.*, 2014, **4**, 593-599.
- 16 O. S. Kwon, S. H. Lee, S. J. Park, J. H. An, H. S. Song, T. Kim and J. Jang, *Adv. Mater.*, 2013, **25**, 4177-4185.
- 17 J. K. McDonough and Y. Gogotsi, *Electrochem. Soc. Interface*, 2013, **22**, 61-66.
- 18 Y. Wang, F. Yan, S. W. Liu, A. Y. S. Tan, H. Song, X. W. Sun and H. Y. Yang, *J. Mater. Chem. A*, 2013, **1**, 5212-5216.
- 19 E. S. Shibu, A. Sonoda, Z. Tao, Q. Feng, A. Furube, S. Masuo and V. Biju, *ACS nano*, 2012, **6**, 1601-1608.
- 20 I. V. Lightcap and P. V. Kamat, *Acc. Chem. Res.*, 2012, **46**, 2235-2243.
- 21 E. Sutter, P. Sutter and Y. Zhu, *Nano Lett.*, 2005, **5**, 2092-2096.
- 22 S. Hore, G. Kaiser, Y.-S. Hu, A. Schulz, M. Konuma, G. Gotz, W. Sigle, A. Verhoeven and J. Maier, *J. Mater. Chem.*, 2008, **18**, 5589-5591.
- 23 J. Wu, W. Shi and N. Chopra, *J. Phys. Chem. C*, 2012, **116**, 12861-12874.
- 24 N. Chopra, J. Wu and L. Summerville, *Carbon*, 2013, **62**, 76-87.
- 25 N. Chopra, L. G. Bachas and M. R. Knecht, *Chem. Mater.*, 2009, **21**, 1176-1178.
- 26 J. Wu, W. Shi and N. Chopra, *Carbon*, 2014, **68**, 708-717.
- 27 X. Peng, and S. S. Wong, *Chem. Mater.*, 2009, **21**, 682-694.
- 28 B. R. Azamian, K. S. Coleman, J. J. Davis, N. Hanson, and M. L. Green, *Chem. Commun.*, 2002, **4**, 366-367.
- 29 M. Olek, M. Hilgendorff, M. Giersig, *Colloids Surf., A*, 2007, **292**, 83-85.
- 30 S. Jeong, H. C. Shim, S. Kim, and C. S. Han, *ACS nano*, 2009, **4**, 324-330.
- 31 B. J. Hinds, N. Chopra, T. Rantell, R. Andrews, V. Gavalas, L. G. Bachas, *Science*, 2004, **303**, 62-65.
- 32 R. S. Mane, S. J. Roh, O. S. Joo, C. D. Lokhande and S. H. Han, *Electrochim. Acta*, 2005, **50**, 2453-2459.
- 33 W. Shi and N. Chopra, *J. Nanopart. Res.*, 2011, **13**, 851-868.
- 34 H. Wei, Y. Su, Z. Han, T. Li, X. Ren, Z. Yang and Y. Zhang, *Nanotechnology*, 2013, **24**, 235706-235712.
- 35 B. T. Draine and P. J. Flatau, *arXiv preprint arXiv* 2013, **307**, 1305-6497.
- 36 W. Shi and N. Chopra, *ACS Appl. Mater. Interfaces*, 2012, **4**, 5590-5607.
- 37 S. Y. Sayed, F. Wang, M. Malac, A. Meldrum, R. F. Egerton, J. M. Buriak, *ACS nano*, 2009, **3**, 2809-2817.
- 38 S. Gilles, C. Kaulen, M. Pabst, U. Simon, A. Offenhäuser and D. Mayer, *Nanotechnology*, 2011, **22**, 295301.
- 39 N. Chopra, W. Shi and A. Bansal, *Carbon*, 2011, **49**, 3645-3662.
- 40 B. Zhao, L. Zhang, X. Wang and J. Yang, *Carbon*, 2012, **50**, 2710-2716.
- 41 M. Majumder, N. Chopra and B. J. Hinds, *J. Am. Chem. Soc.*, 2005, **127**, 9062-9070.
- 42 J. Wu and N. Chopra, *Ceram. Trans.*, 2012, **238**, 17-29.
- 43 H. Wang, Q. W. Chen, J. Chen, B. X. Yu, X. Y. Hu, *Nanoscale*, 2011, **3**, 4600-4603.
- 44 Y. Li and N. Chopra, *Carbon*, 2014, **77**, 675-687.
- 45 H. Ago, T. Kugler, F. Cacialli, W. R. Salaneck, M. S. Shaffer, A. H. Windle and R. H. Friend, *J. Phys. Chem. B*, 1999, **103**, 8116-8121.
- 46 M. C. Hsiao, S. H. Liao, M. Y. Yen, C. C. Teng, S. H. Lee, N. W. Pu and M. H. Hsiao, *J. Mater. Chem.*, 2010, **20**, 8496-8505.
- 47 G. D. Nessim, A. J. Hart, J. S. Kim, D. Acquaviva, J. Oh, C. D. Morgan and C. V. Thompson, *Nano Lett.*, 2008, **8**, 3587-3593.
- 48 C. Bittencourt, C. Navio, A. Nicolay, B. Ruelle, T. Godfroid, R. Snyders and C. P. Ewels, *J. Phys. Chem. C*, 2011, **115**, 20412-20418.
- 49 Y. Li and N. Chopra, *Mater. Res. Soc. Res. Proc.*, 2013, **1572**, mrs13-1572
- 50 U. J. Kim, C. A. Furtado, X. Liu, G. Chen and P. C. Eklund, *J. Am. Chem. Soc.*, 2005, **127**, 15437-15445.
- 51 M. C. Chang and J. Tanaka, *Biomaterials*, 2002, **23**, 4811-4818.
- 52 R. Zeng, R. Shen, Y. Zhao, X. Li, Z. Sun and Y. Shen, *Nanotechnology*, 2014, **25**, 135602.
- 53 C. Shan, H. Yang, D. Han, Q. Zhang, A. Ivaska and L. Niu, *Bioelectron*, 2010, **25**, 1070-1074.
- 54 V. Biju, T. Itoh, A. Anas, A. Sujith and M. Ishikawa, *Anal. Bioanal. Chem.*, 2008, **391**, 2469-2495.
- 55 C. Ünlü, G. Ü. Tosun, S. Sevim and S. Özçelik, *J. Mater. Chem. C*, 2013, **1**, 3026-3034.
- 56 M. Y. Nadeem and W. Ahmed, *Turkish J. Phys.*, 2009, **24**, 651-659.
- 57 S. Zhu, T. P. Chen, Y. C. Liu, Y. Liu and S. A. Fung, *J. Nanopart. Res.*, 2012, **14**, 1-6.

- 58 K. Yamada, K. Miyajima and F. Mafuné, *J. Phys. Chem. C*, 2007, **111**, 11246-11251.
- 59 Y. Li and N. Chopra, *Mater. Res. Soc. Res. Proc.*, 2014, **1700**, mrss14-1700.
- 60 C. F. Bohren and D. R. Huffman, *John Wiley & Sons*, 2008, **130**.
- 61 M. Grätzel, *Nature*, 2001, **414**: 338-344.
- 62 H. D. Cho, A. S. Zakirov, S. U. Yuldashev, C. W. Ahn, Y. K. Yeo and T. W. Kang, *Nanotechnology*, 2012, **23**, 115401.
- 63 S. Esplugas, J. Gimenez, S. Contreras, E. Pascual and M. Rodríguez, *Water Res.*, 2002, **36**, 1034-1042.
- 64 I. Mora-Seró, S. Gimenez, F. Fabregat-Santiago, R. Gomez, Q. Shen and T. J. Toyoda, *Acc. Chem. Res.*, 2009, **42**, 1848-1857.
- 65 G. R. Vela, and J. R. Ralston, *Can. J. Microbiol.*, 1978, **24**, 1366-1370.
- 66 Y. Zhou, G. Chen, Y. Yu, Y. Feng, Y. Zheng, F. He, and Z. Han, *Phys. Chem. Chem. Phys.*, 2015, **17**, 1870-1876.
- 67 X. Fan, G. Zhang, and F. Zhang, *Chem. Soc. Rev.* 2015, in press
- 68 N. Soltani, E. Saion, M. Z. Hussein, M. Erfani, A. Abedini, G. Bahmanrokh and P. Vaziri, *Int. J. Mol. Sci.*, **13**, 12242-12258.
- 69 S. Guo, D. Bao, S. Upadhyayula, W. Wang, A.B. Guvenc, J.R. Kyle, M. Ozkan, *Adv. Func. Mater.*, 2013, **23**, 5199-5211.